Bilayer Haldane model: From trivial band insulator to fractionalized quantum anomalous Hall insulator

Sopheak Sorn[*]

Department of Physics, University of Toronto, Toronto, Ontario M5S 1A7, Canada

Motivated by work on the bulk topological proximity effect and the topological bootstrap, we consider two coupled layers of quantum anomalous Hall (QAH) insulators with opposite signs of time-reversal breaking, which leads to a trivial band insulator at half-filling. We study the impact of interactions in this model within slave rotor theory, which leads to a layer-selective Mott transition, resulting in a fractionalized quantum anomalous Hall insulator QAH* where a Chern band insulator coexists with a chiral spin liquid. We also compute the edge electron spectral function in the vicinity of the QAH* phase.

I. INTRODUCTION

Recent theoretical work on topological phases of matter has introduced the concept of a "bulk topological proximity effect" (BTPE) [1], wherein a topologically trivial layer coupled to topologically nontrivial bands [2] can itself exhibit nontrivial topological character of the *opposite* type. This arises from virtual hopping transitions into the nontrivial layer. An interesting variant of this idea, which was subsequently explored, is the "topological bootstrap" [3], where isolated spins can be driven into a topologically ordered chiral spin liquid phase [4–8] via Kondo coupling to nontrivial Chern bands [9]. Naively we expect that increasing the strength of the Kondo coupling might lead to a transition into a trivial insulator, where every spin binds an electron.

In a different research trend studying the effects of electron correlation on band topology, new correlation-driven phases of matter have been found with and without spontaneously broken symmetries [10–12], e.g., antiferromagnetic Chern insulators [13] and fractionalized topological insulators with neutral gapless surface excitations [14,15]. Motivated by the rich physics of such phases and to explore the connection between BTPE and the topological bootstrap, we study a toy bilayer Haldane model, where each layer hosts spin-1/2 electrons in topologically nontrivial phases but which are of the opposite type. At half-filling, the total Chern number of the occupied "valence" bands is then zero. We assume that one of the layers could have a bandwidth reduced by a factor $0 < \lambda < 1$. For small $\lambda \ll 1$, we may view one of these layers as having inherited its nontrivial "opposite" band topology due to the BTPE. In this setting we study how tuning Hubbard interactions in one layer eventually leads to a chiral spin liquid Mott insulator which effectively decouples from the other layer, so that the net combination acts as a fractionalized quantum anomalous Hall insulator QAH*, which has bulk semions and topological order coexisting with a quantum Hall effect. Such a system would have chiral charge edge modes and a counterpropagating neutral edge mode, so that it

would exhibit a quantized thermal Hall effect and a quantized electrical Hall effect which violate the Wiedemann-Franz law. For $\lambda \ll 1$, this QAH* phase is identifiable as that obtained within the topological bootstrap picture.

QAH* is analogous to the fractionalized Fermi liquid FL* studied in Ref. [16], in which a spin liquid coexists with a Fermi liquid. It is distinct from a correlated Chern insulator phase CI* [17] obtained within the slave spin theory of a single-layer Chern insulator. The CI* phase also possesses fractionalized quasiparticles and exhibits a quantized charge Hall effect, yet it has no electronlike quasiparticles in contrast to QAH*. In the language of Ref. [18], the CI* may be viewed as an "orthogonal" QAH insulator.

We have explored the phase diagram of this bilayer model within a slave rotor mean-field theory calculation [19–23]. In the presence of inversion symmetry, the valence bands have Chern numbers ±1, while incorporating inversion breaking terms renders each valence band to individually have Chern number zero. As opposed to the Kondo lattice model explored in the context of the topological bootstrap, this model can be viewed as a periodic Anderson model in which a layer-selective Mott transition leads to the QAH* phase. However, simply increasing correlations on one layer does not necessarily directly drive the system into the QAH* phase since the correlated bands tend to drift up in energy with increasing interaction strength and thus get progressively depopulated; we thus generically need an additional bias potential in order to convert the correlated layer into a half-filled Mott insulator. Finally, in addition to the above discussed trivial band insulator and QAH* phases, we find wide regimes of Chern metal and new Dirac semimetal phases.

We compute the edge electron spectral function in the correlated trivial band insulator as we approach the QAH* phase. Deep in the trivial band insulator regime, there are counterpropagating electronic edge modes which hybridize and gap out. However, closer to the QAH* phase, this hybridization strongly decreases. Furthermore, we find that while the chiral edge mode emanating from the noninteracting layer has high spectral intensity, the counterpropagating edge mode has a diminished intensity which is progressively weakened upon approaching the layer Mott transition. Thus, although the

*ssorn@physics.utoronto.ca

correlated band insulator is topologically trivial, its spectral function signature close to the QAH* phase may be (incorrectly) suggestive of a topologically nontrivial state. In the QAH* phase, the edge modes decouple.

The phase diagram is summarized in Fig. 3 and is the focus of the rest of this paper. Before we turn to this, it is important to note that while our results indicate the type of phases which might arise in the presence of correlations, additional interactions may be needed to stabilize the QAH* phase in this specific microscopic model [24] once we allow for competition with spontaneous magnetically ordered phases. The paper is organized as follows. Section II outlines the model Hamiltonian and its symmetries. Section III discusses its noninteracting phase diagram. Section IV discusses the results from a slave rotor theory of the interactions, using a nonlinear sigma model approach to the rotor fluctuations, and presents numerical results for the edge electron spectral function.

II. MODEL AND SYMMETRIES

A. Bilayer Hamiltonian

The bilayer Hamiltonian we study consists of three parts: a Haldane model on each layer, an interlayer hopping term which hybridizes the Chern bands of the individual layers, and a Hubbard interaction which drives a Mott transition on one layer, so that

$$H = H_1 + \lambda H_2 + H_{\text{hyb}} + H_2^{\text{int}}. \tag{1}$$

Here H_1 and H_2 denote the noninteracting hopping Hamiltonian on layers 1 and 2, respectively. The bands of layer 2 are rescaled with respect to layer 1 by a parameter $\lambda < 1$. Let us denote the electron operators on layer 1 and layer 2 as $c^\dagger$ and $d^\dagger$, respectively. The noninteracting layer-1 Hamiltonian $H_1 \equiv H_{\text{Haldane}}(t_1, t_2, \phi, M)$ is the honeycomb lattice Haldane model Hamiltonian [25]

$$H_{\text{Haldane}} = -\sum_{\langle ij \rangle, \sigma} t_1 c_{i\sigma}^\dagger c_{j\sigma} - \sum_{\langle\langle ij \rangle\rangle, \sigma} t_2 e^{-i v_{ij} \phi} c_{i\sigma}^\dagger c_{j\sigma} + \text{H.c.}$$
$$+ M \sum_{i\sigma} \epsilon_i c_{i\sigma}^\dagger c_{i\sigma}, \tag{2}$$

while $H_2 \equiv H_{\text{Haldane}}(t_1, t_2, -\phi, M)$ with fermion operators $c^\dagger \to d^\dagger$. Here $\sigma = \uparrow, \downarrow$ labels spin, and $\epsilon_i = \pm 1$ labels the respective sublattices A and B so that M controls the breaking of the two-dimensional (2D) inversion symmetry. The second-neighbor hopping term breaks time-reversal symmetry (TR). As shown in Fig. 1, $v_{ij} = \pm 1$, which results in an alternating flux profile with a vanishing total flux through each hexagon. Here and below we will set $t_1 = 1$.

The hybridization Hamiltonian H_{hyb} encapsulates interlayer hopping (which is momentum independent), and a layer bias potential Δ:

$$H_{\text{hyb}} = -t_\perp \sum_{i\sigma} (c_{i\sigma}^\dagger d_{i\sigma} + \text{H.c.}) - \Delta \sum_{i\sigma} d_{i\sigma}^\dagger d_{i\sigma}. \tag{3}$$

Electron-electron interactions are encoded in H_2^{int}, which is the on-site Hubbard repulsion; for simplicity, we have
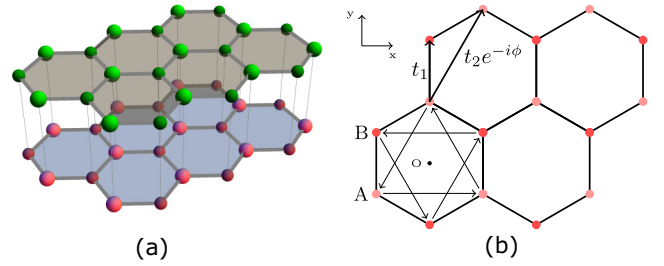

FIG. 1. (a) Bilayer honeycomb lattice showing vertical AA stacking. (b) Bottom layer (layer 2) depicting first- and second-neighbor hoppings t_1 and t_2. The second-neighbor hopping is complex, given by $t_2 e^{-i v_{ij} \phi}$, and arrows in the lowest left plaquette denote the directions of positive $v_{ij} = +1$, where $v_{ji} = -v_{ij}$. The top layer (layer 1) has reversed sign of v_{ij}.

assumed that this interaction is only present on layer 2:

$$H_2^{\text{int}} = U \sum_i n_{d,i,\uparrow} n_{d,i,\downarrow}, \tag{4}$$

where $n_{d,i,\sigma} = d_{i\sigma}^\dagger d_{i\sigma}$. Such a Hubbard repulsion will drive a Mott transition in layer 2. When $\lambda < 1$, meaning the two layers are *inequivalent*, with layer 2 having a smaller bandwidth, turning on a Hubbard interactions in both layers will drive a similar layer-selective Mott transition in layer 2.

B. Symmetries

The bilayer Haldane model has the following symmetries: (1) translational symmetry of the honeycomb lattice; (2) C_3 spatial rotation symmetry about the center of each hexagonal plaquette; (3) SU(2) spin rotation symmetry; (4) while time-reversal symmetry $\mathcal{T}$ (i.e., complex conjugation which reverses flux $\phi \to -\phi$) is broken, $\mathcal{T}M$ which combines it with a mirror operation $\mathcal{M}$ is a good symmetry. Here the mirror line connects opposite vertices of the hexagon. (5) Finally, when $M = 0$, there is 2D inversion symmetry, which is equivalent to π rotation about the hexagon center; it sends the momentum $\mathbf{k} \mapsto -\mathbf{k}$ and exchanges the two sublattices.

III. NONINTERACTING PHASE DIAGRAM

Before studying the effects of interaction, we compute the noninteracting phase diagram of the bilayer.

When $t_\perp = 0$, the two layers are decoupled. In this limit, for $t_2, \phi \neq 0$ and when $|M/t_2| < 3\sqrt{3}|\sin\phi|$, each band in each layer carries a nontrivial Chern number, resulting in a quantum anomalous Hall effect at half-filling, while larger $|M/t_2|$ results in a trivial band insulator [25]. However, the fact that the phase ϕ in layer 2 is negative of that in layer 1 renders the whole system topologically trivial even when $M = 0$.

Here, and below, we fix the density to be at half-filling, and set $t_2 = 0.25$, $t_\perp = 0.3$, and $\phi = \pi/2$, and explore the phase diagram as we tune M and Δ for $\lambda = 0.5$. We discover three phases.

(1) A trivial band insulator such that the total Chern number of occupied bands is zero. However, bands below the Fermi level (i.e., valence bands) may carry individually either nonzero Chern numbers or zero Chern number. We notice that
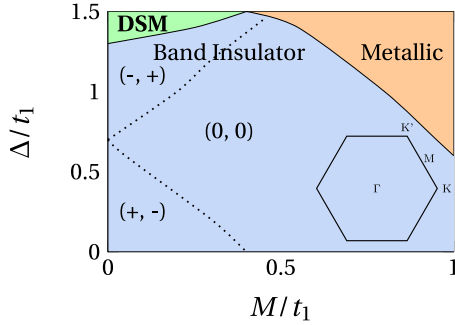
FIG. 2. Noninteracting phase diagram for $t_\perp = 0.3t_1$ and $\lambda = 0.5$. The band insulator is subdivided into three categories characterized by the Chern numbers of the valence bands. The $(0, 0)$ phase dominates and is present only with a nonzero M. The Dirac semimetal has six Dirac cones in the BZ with the Fermi level at the Dirac points. These Dirac points can be gapped out by further hopping, e.g., third-nearest-neighbor hopping. The metallic phase arises from the effect of large M which causes the band to have extrema in the vicinity of the K and K' points. At half-filling, the band structure has electron pockets around K points and hole pockets around K' points.

individually trivial valence bands with Chern numbers $(0, 0)$ can only be achieved when $M \neq 0$.

(2) As one increases the strength of Δ, the band insulator gives way to a Dirac semimetal with six-band touching points in the Brillouin zone (BZ). The Dirac cones emerge pairwise from each M point, and move towards towards the Γ point. When $M = 0$, the Dirac cones are situated perfectly on the Γ-M lines but are otherwise rotated away. This can be understood as a mathematical structure of the Bloch Hamiltonian, see Appendix A. The Dirac cones are, however, not protected by any symmetry and can be gapped out, for instance, by introducing a third-nearest-neighbor hopping.

(3) Upon increasing M, the phase diagram shows an ambipolar metallic phase with no Dirac band touching points, but with electron pockets and hole pockets around the K and K' points, respectively.

In the rest of the paper we use slave rotor theory to study the effect of interactions on the phase diagram in Fig. 2. We will mainly explore the impact of varying U and Δ, for different values of M, starting from noninteracting phases which are predominantly topologically trivial. This corresponds to starting from vertical cuts through the noninteracting phase diagram and varying U.

IV. SLAVE ROTOR MEAN-FIELD THEORY

A. Slave rotor representation

Slave rotor representation has been used in studying Mott insulating phases and Mott transitions in strongly correlated systems [19–23]. Here we make use of this representation to study a layer-selective Mott transition in the interacting bilayer model. In this representation the electron operator in the correlated layer 2 is decomposed as $d^\dagger_{i\sigma} = f^\dagger_{i\sigma} e^{-i\theta_i}$, into a fermionic spinon operator $f^\dagger_{i\sigma}$ and a rotor operator $e^{-i\theta_i}$ which, respectively, carry the spin and charge degrees of freedom of the electron. To project this expanded Hilbert

space back to the physical electron Hilbert space, we need to impose the local constraint

$$n_{fi} + L_i - 1 = 0. \tag{5}$$

Electron hopping terms in H_2 can be recast in the form $f^\dagger_{i\sigma} f_{j\sigma} e^{-i\theta_i} e^{i\theta_j}$, while the hybridization term becomes

$$H_{\text{hyb}} = -\sum_{i\sigma} t_\perp f^\dagger_{i\sigma} e^{-i\theta_i} c_{i\sigma} + \text{H.c.} - \Delta \sum_{i\sigma} f^\dagger_{i\sigma} f_{i\sigma}. \tag{6}$$

The Hubbard interaction term is written as

$$H_2^{\text{int}} = \frac{U}{2} \sum_i \left(L_i^2 + n_{fi} - 1\right), \tag{7}$$

where we have used the relation

$$n_{di\uparrow} n_{di\downarrow} = n_{di}(n_{di} - 1)/2 = \left(L_i^2 + n_{fi} - 1\right)/2, \tag{8}$$

which is valid when the constraint in Eq. (5) is obeyed.

B. Mean-field theory

To make progress, we consider the following mean-field decoupling of the spinon-rotor interaction terms:

$$f^\dagger_{i\sigma} f_{j\sigma} e^{-i\theta_i} e^{i\theta_j} \approx \langle f^\dagger_{i\sigma} f_{j\sigma} \rangle e^{-i\theta_i} e^{i\theta_j} + f^\dagger_{i\sigma} f_{j\sigma} \langle e^{-i\theta_i} e^{i\theta_j} \rangle$$
$$- \langle f^\dagger_{i\sigma} f_{j\sigma} \rangle \langle e^{-i\theta_i} e^{i\theta_j} \rangle, \tag{9}$$

$$f^\dagger_{i\sigma} c_{i\sigma} e^{-i\theta_i} \approx \langle f^\dagger_{i\sigma} c_{i\sigma} \rangle e^{-i\theta_i} + f^\dagger_{i\sigma} c_{i\sigma} \langle e^{-i\theta_i} \rangle$$
$$- \langle f^\dagger_{i\sigma} c_{i\sigma} \rangle \langle e^{-i\theta_i} \rangle, \tag{10}$$

where the expectation values $\langle \cdots \rangle$, dubbed "bond mean fields," are to be determined self-consistently. This decoupling scheme splits the Hamiltonian into two parts: one involving coupled spinons and c electrons, and the other involving rotors. Equivalently, the many-body electron wave function is then of the form

$$|\Psi_{\text{MF}}\rangle = |\Psi_{fc}\rangle \otimes |\Psi_\theta\rangle, \tag{11}$$

where $|\Psi_{fc}\rangle$ is the coupled spinon and c-electron wave function and $|\Psi_\theta\rangle$ is the rotor wave function, with the constraint in Eq. (5) being imposed on average.

Here we will focus on mean-field ground states which do not break any symmetries of the model Hamiltonian, so we consider a "uniform" ansatz. In this case, the bond mean fields are parametrized by only a few parameters. For nearest-neighbor bonds,

$$\langle f^\dagger_{i\sigma} f_{j\sigma} \rangle = F_{nn}, \tag{12}$$

$$\langle e^{-i\theta_i} e^{i\theta_j} \rangle = X_{nn}, \tag{13}$$

where F_{nn} and X_{nn} are real valued and identical on all bonds due to the combination of translation, C_3, and $\mathcal{T}M$ symmetries. (Note that in the slave rotor representation, $\mathcal{T}$ sends $f_{i\sigma} \rightarrow f_{i\sigma}$, $e^{\pm i\theta_i} \rightarrow e^{\pm i\theta_i}$, and conjugates complex numbers). For next-nearest neighbors, there are two distinct bond mean fields corresponding to the two sublattices:

$$\langle f^\dagger_{i\sigma} f_{j\sigma} \rangle = F_{nnn,A(B)} e^{-i\nu_{ij}\varphi_{A(B)}}, \tag{14}$$

$$\langle e^{-i\theta_i} e^{i\theta_j} \rangle = X_{nnn,A(B)} e^{-i\nu_{ij}\eta_{A(B)}}. \tag{15}$$

The bond mean fields for the interlayer term are

$$\langle f_{i\sigma}^{\dagger} c_{i\sigma} \rangle = F_{\perp, A(B)}, \tag{16}$$

$$\langle e^{i\theta_i} \rangle = \bar{X}_{A(B)}. \tag{17}$$

They can be chosen to be real valued. We impose the constraint (5) on average by introducing two Lagrange multipliers λ_A and λ_B for the two sublattices. The mean-field theory now amounts to self-consistently solving separate rotor and coupled spinon-c Hamiltonians H_{θ} and H_{fc}, respectively.

C. Fermionic and rotor Hamiltonians

The fermionic part of the mean-field Hamiltonian, involving c and f, is given by

$$H_{fc} = H_1 + \lambda H_{2,f} + H_{\text{hyb},f} + \frac{U}{2} \sum_i n_{f,i}$$
$$+ \sum_i \lambda_i n_{f,i} - \mu \sum_i (n_{f,i} + n_{c,i}), \tag{18}$$

where the second to last term comes from the constraints (5), and the last term is the chemical potential, used to impose the electron density at half-filling. H_1 is unaltered, while the rest is given below:

$$H_{2,f} = - \sum_{\langle ij \rangle, \sigma} t_1 X_{nn} f_{i\sigma}^{\dagger} f_{j\sigma} + \text{H.c.}$$
$$- \sum_{\langle\langle ij \rangle\rangle \sigma} t_2 X_{nnn,i} e^{-i\nu_{ij}\eta_i} e^{-i\nu_{ij}\phi} f_{i\sigma}^{\dagger} f_{j\sigma} + \text{H.c.}$$
$$+ M \sum_{i\sigma} \epsilon_i f_{i\sigma}^{\dagger} f_{i\sigma}, \tag{19}$$

$$H_{\text{hyb},f} = - \sum_{i\sigma} (t_\perp \bar{X}_i f_{i\sigma}^{\dagger} c_{i\sigma} + \text{H.c.}) - \Delta \sum_i n_{f,i}. \tag{20}$$

We can now compute the ground state and the expectation values in (12)–(17) in order to solve the fermionic sector, and then evaluating averages F_{nn} and F_{nnn}.

The rotor Hamiltonian is given by

$$H_{\theta} = - \sum_{\langle ij \rangle} 2\lambda t_1 F_{nn} X_i^{\dagger} X_j + \text{H.c.}$$
$$- \sum_{\langle\langle ij \rangle\rangle} 2\lambda t_2 F_{nnn,i} e^{-i\nu_{ij}(\phi+\varphi_i)} X_i^{\dagger} X_j + \text{H.c.}$$
$$- \sum_i 2t_\perp F_{\perp,i} X_i^{\dagger} + \text{H.c.} + \frac{U}{2} \sum_i L_i^2 + \sum_i \lambda_i L_i, \tag{21}$$

where the operator $X_i \equiv e^{i\theta_i}$. The factors of 2 arise from spin sums in the spinon sector.

To solve for the ground state expectation values in (12)–(17), we integrate out the angular momentum and resort to a nonlinear sigma model representation of the rotor Hamiltonian which we treat at Gaussian level as an approximation. This last step involves solving a quadratic action in the sigma field, which can then be used to compute the bond mean fields (see Appendix B for more details).

A useful quantity in this approach is the expectation value $\langle X_i \rangle$ which distinguishes a Mott insulating phase from a non-

Mott phase. When $\langle X_i \rangle$ vanishes, the charge fluctuation is strongly suppressed, which entails a Mott insulating phase. On the contrary, nonvanishing $\langle X_i \rangle$ leads to charge fluctuations and describes non-Mott phases, which can still be insulating depending on whether the fermionic spectrum is gapped.

V. RESULTS

A. Interacting phase diagram

The results of slave rotor theory are summarized in Fig. 3 where we plot phase diagrams of the bilayer Haldane model as we vary the interaction strength U and the bias potential Δ. The six panels in Fig. 3 correspond to different sets of M and λ. We find the following phases: (1) band insulator, (2) Dirac semimetal, (3) Chern metal, and (4) fractionalized quantum anomalous Hall insulator (QAH*). Their properties are described below. In our discussion of the band structure, note that each band is doubly degenerate in spin; below we will describe one spin species unless otherwise mentioned explicitly.

1. Band insulator

The noninteracting model is a trivial band insulator, and it continues to be a stable phase in a regime of the phase diagram at smaller U. In this phase, $\langle X \rangle \neq 0$, so the electrons in layer 2 are still well-defined excitations. The Chern numbers of the valence bands are shown in the parentheses; they sum up to zero so the insulator is topologically trivial. The dashed lines separate three ground states with distinct Chern numbers $(-1, +1)$, $(+1, -1)$, and $(0, 0)$. This distinction is useful in understanding the effects the inversion breaking term and the evolution of the Chern bands across phase transitions. Δ and U tend to push the bands up or down in energy relative to one another, causing band touchings and Chern number exchanges among the valence bands. (Note that these gap closings occur between different valence bands, and not between valence and conduction bands, so the system always remains a band insulator.) In the presence of inversion symmetry, as in Figs. 3(a)–3(c), the gap closings occur at an even number of Dirac points, which results in a change in Chern number by $\Delta C = \pm 2$ in each band. Without inversion symmetry, as in Figs. 3(d)–3(f), the gap closings take place at an odd number of Dirac points so that the Chern number of each valence band can change by $\Delta C = \pm 1$ across the transitions.

2. Dirac semimetal (DSM)

The DSM features six Dirac points in the BZ. Figure 4 illustrates a band structure of the DSM. It describes the spectrum of the spinons hybridized with the electrons from layer 1 due to $\langle X \rangle \neq 0$ (so that spinons in layer 2 have a nonzero overlap with electrons.) The Dirac points sit on the Γ-M lines in the BZ when $M = 0$. The inversion symmetry breaking term can move the Dirac points off the high symmetry lines. The transition from a band insulator to the DSM proceeds with the formation of gapless points at the BZ boundary (M points), each of which then splits into a pair of Dirac cones moving towards the Γ point. Similar to Weyl-Kondo semimetals [26], the DSM phase arises from strong correlations, yet it is not as robust and can be gapped out without breaking
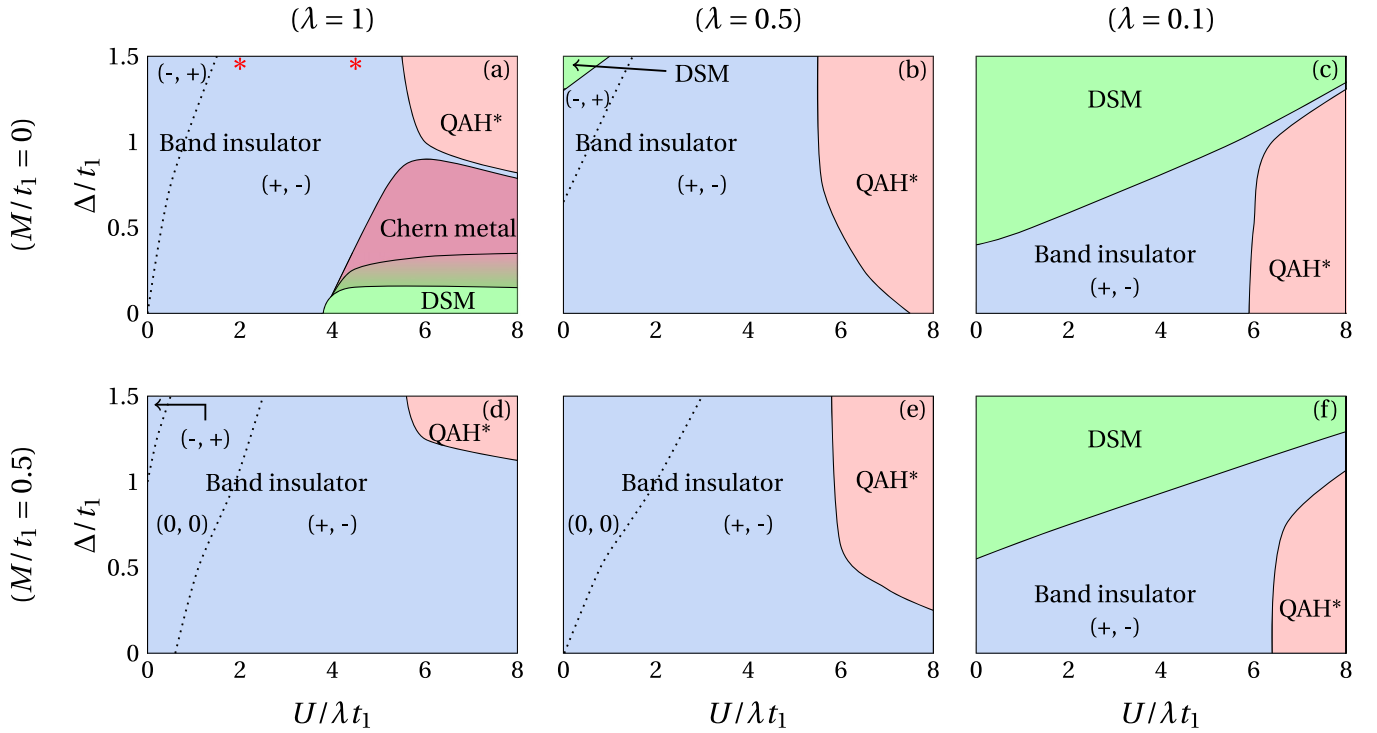
FIG. 3. Phase diagrams of the Haldane bilayer model obtained using slave rotor mean-field theory as a function of the interaction strength $U/\lambda t_1$ and the bias potential Δ/t_1. (a)–(c) Inversion-symmetric cases, while inversion symmetry is absent in (d)–(f). Here $\lambda < 1$ is the bandwidth scaling factor of the correlated layer and M is the degree of inversion symmetry breaking. There are five phases in total: Band insulator phases which we distinguish by indicated Chern numbers for the valence bands, a Dirac semimetal (DSM), a Chern metal with electron and hole pockets, an intermediate metallic phase between the preceding two with the coexistence of Dirac cones and pockets (shown as the color gradient between the Chern metal and the DSM), and a fractionalized quantum anomalous Hall phase (QAH*) in which the correlated layer undergoes a layer-selective Mott transition. The two stars in the upper left panel mark the points in the parameter space where we compute the electron spectral functions in Sec. V.

any symmetries, e.g., by introducing third-nearest-neighbor hopping terms.

3. Chern metal

In this phase the band structure acquires electron pockets around M points and hole pockets around K and K' points

as shown in Fig. 5, so it is a compensated metal. Each band carries a nontrivial Chern number, which can lead to a finite Hall conductivity. A band structure calculation of the fermionic Hamiltonian on a cylinder with zigzag edges reveals no edge mode at the Fermi level, yet there are edge modes far below the Fermi level which start from the lower valence band and merge into the upper valence bands.
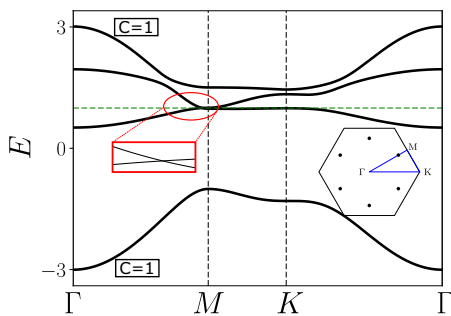

FIG. 4. Fermionic band structure depicting the hybridized spectrum of electrons from layer 1 with spinons from layer 2 in the DSM phase (having $\langle X \rangle \neq 0$). The DSM has six Dirac points lying on the Γ-M lines of the BZ as shown in the inset. The data is obtained at $M = 0$, $\lambda = 1$, $\Delta = 0$, $U = 6t_1$, and $t_1 = 1$ in the upper left panel of Fig. 3.
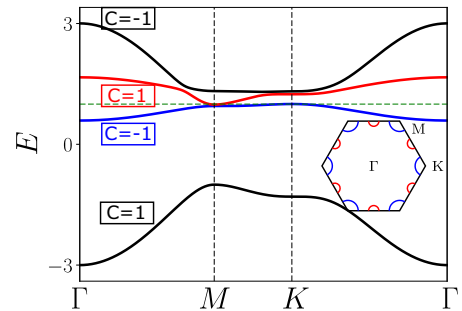

FIG. 5. Fermionic band structure depicting the hybridized spectrum of electrons from layer 1 with spinons from layer 2 in the Chern metal phase where $\langle X \rangle \neq 0$. The Fermi level passes through a valence band and a conduction band, giving rise to hole pockets and electron pockets (see the inset: red for electron pockets and blue for the hole pockets.) The data is obtained at $M = 0$, $\lambda = 1$, $\Delta = 0.5t_1$, $U = 7t_1$, and $t_1 = 1$.

The transition into the Chern metal can proceed in two ways from either a band insulator or a DSM. Starting from the band insulator, the band structure acquires electron and hole pockets and becomes a Chern metal. On the other hand, the transition from DSM passes through an intermediate metallic phase with electron and hole pockets coexisting with Dirac cones. This phase is denoted by a color gradient in the upper left panel in Fig. 3. The Chern metal phase appears after the Dirac cones merge and gap out at the BZ boundary.

4. Fractionalized quantum anomalous Hall insulator

This phase corresponds to a Mott phase in layer 2 in which the spin and charge of the correlated electrons dissociate. This kills the interlayer hybridization, resulting in an effective decoupling between the two layers. Layer 1 is characterized by a nontrivial band topology with a bulk gap, electronlike excitations, and chiral electronic edge modes. The total Chern number is $+2$ (counting both spins) which results in the quantization of electrical and thermal Hall conductivities [27]. Layer 2 is described by a Mott phase with a topologically nontrivial spinon band structure. This corresponds to a topologically ordered chiral spin liquid as studied in Ref. [28]. The chiral spin liquid has a gapped bulk spectrum, semion quasiparticles, and a chiral neutral gapless edge mode [4,5]. To understand the neutral edge mode, one needs to go beyond the mean-field treatment. The mean-field spinon Hamiltonian suggests two spinon edge modes, but the ground state of the slave rotor can still have a finite overlap with unphysical states [those which violate the constraint (5)]. Thus, one needs to consider a projection onto the physical Hilbert space. As argued in Ref. [29], the two spinon modes can be identified with a gapless charged mode and a gapless neutral mode, the former of which will be gapped out upon the projection, leaving only one gapless neutral mode at the boundary. Its neutrality leads to a zero contribution to the electrical Hall effect while contributing a quantized thermal Hall conductivity of one unit quantum [27].

The properties of the total system can be summarized below. In the bilayer, the quasiparticle excitations consist of electrons and semions. At the boundary, there are gapless chiral charged modes and a counterpropagating neutral mode. The total electric Hall conductivity is $\sigma_{xy} = 2\frac{e^2}{h}$ which solely arises from layer 1, while the thermal Hall conductivity κ_H equals to $+1$ quantized unit of the Hall conductivity ($+2$ and -1 from layer 1 and layer 2, respectively). The relation between κ_H and σ_{xy} violates the Wiedemann-Franz law without having a vanishing or a fractional electric Hall conductivity (like those in spin liquids and fractional quantum Hall liquids [30]). QAH* is similar to fractionalized Fermi liquids (FL*), proposed in Ref. [16], in which the spins and the electrons of a Kondo lattice model are effectively decoupled, where spins are fractionalized and form a spin liquid phase, while the electrons form a Fermi liquid.

We have found that the QAH* phase occupies a significant portion of the phase diagram. In the topological bootstrap limit $\lambda \ll 1$, the QAH* phase can arise straightforwardly—without the bias potential—upon increasing the interaction strength. When one increases the strength of M, the phase diagram changes quantitatively in that the QAH* phase is
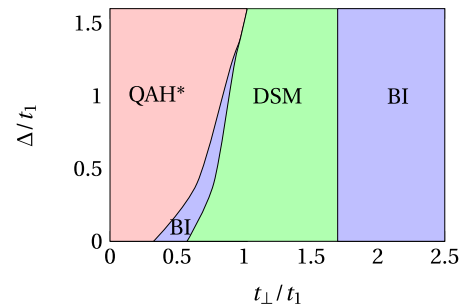

FIG. 6. A phase diagram depicting the effects of hybridization $t_\perp$ on QAH*. The system becomes a trivial band insulator (BI) at large hybridizations, which is identifiable with a Kondo insulator in the strong-coupling limit. The two BI regions are physically the same in terms of their Chern numbers and the presence of a gap in the band structure. The intermediate Dirac semimetal phase may be gapped out upon adding other microscopic terms. Thus it is possible to have a direct transition from QAH* into BI. (The phase diagram is obtained at $U = 8.0\lambda t_1$, $\lambda = 0.5$, $M = 0$.)

pushed to the right as one requires a larger U to drive the system into a Mott phase on account of an increased tendency to a charge imbalance between the two sublattices. As one departs from the topological bootstrap limit, a Mott phase requires a bias potential $\Delta > 0$ to compensate for the energy cost by the Hubbard interactions in order to hold electrons in layer 2 to a half-filled density.

Upon increasing the strength of the hybridization $t_\perp$, the system passes through intermediate phases before eventually becoming a topologically trivial band insulator (BI). The phase diagram in Fig. 6 illustrates the hybridization effects on QAH*. The intermediate phase—being a DSM—can be gapped out by adding other microscopic terms to the Hamiltonian. Thus it is possible for QAH* to have a direct transition into the BI phase.

A similar hybridization effect has been studied in a periodic Anderson model as a Kondo lattice model [31], wherein topological bands are coupled to localized f electrons. As a function of the hybridization strength, the system undergoes a quantum phase transition from a Z_2 topological insulator to a trivial Kondo insulator. In the topological insulator phase, the conduction electrons and the localized electrons are effectively decoupled, in analogy with the case of QAH*. After the hybridization exceeds a threshold, the system becomes a Kondo insulator. This phase is analogous to the BI phase in Fig. 6. The existence of the threshold is attributed to the gap in the spectrum of the conduction electrons in the Kondo lattice model [a role played in our case by the gap in the spectrum of H_1 from Eq. (1)] with the strength of the critical hybridization set by this gap.

B. Edge electron spectral function

The ground state wave function in slave rotor mean-field theory is a direct product of spinon and rotor wave functions, which allows us to determine the electron Green function $G_d(x, \tau) \equiv \langle T_\tau d_x(\tau) d_0^\dagger(0) \rangle$. In real space, G_d is the product of spinon and rotor Green functions, $G_d(x, \tau) = G_f(x, \tau) G_X(x, \tau)$, so in momentum space it becomes a
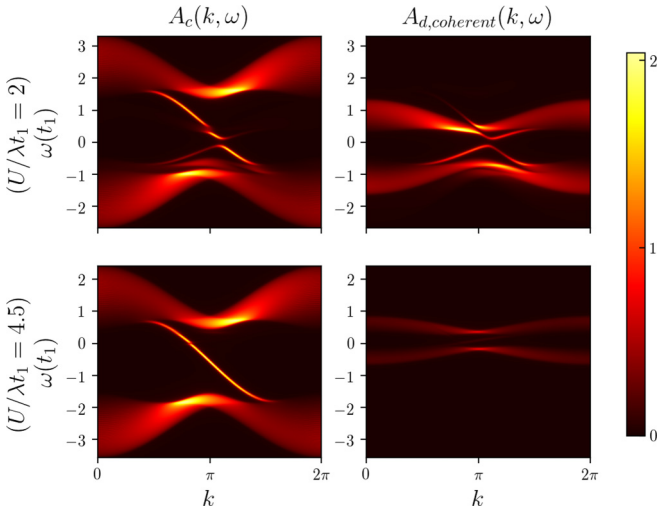
FIG. 7. Spectral functions of electrons in layer 1 and layer 2 (left and right columns) near a zigzag boundary of a cylinder at $U = 2t_1$ (deep in the band insulator phase) and $U = 4.5t_1$ (close to the transition to QAH*), marked by stars in Fig. 3(a) with $\Delta = 1.5t_1$. Away from the transition, the hybridization is still profound, so the edge modes from layer 1 and layer 2 are hybridized, leading to a gap at $\omega = 0$. One can still identify the remnant of a left moving edge mode in the upper left panel and a right moving edge mode in the upper right panel. On the contrary, as the system approaches the QAH*, the coherent part of the spectral function of the correlated electron fades away since the hybridization is increasingly suppressed, leaving A_c almost unaffected.

convolution:

$$G_d(\mathbf{k}, i\omega_n) = \sum_{\mathbf{q}, i\Omega_n} G_f(\mathbf{q}, i\Omega_n) G_X(\mathbf{k} - \mathbf{q}, i\omega_n - i\Omega_n).$$

(22)

Here $G_X(\mathbf{p}, i\nu_n) = Z\delta_{\mathbf{p},0}\delta_{\nu_n,0} + \tilde{G}_X(\mathbf{p}, i\nu_n)$, where the first part is the contribution from zero momentum and frequency $Z \sim |\langle X_i \rangle|^2$. Then $G_d(\mathbf{k}, i\omega_n) = ZG_f(\mathbf{k}, i\omega_n) + \tilde{G}_d(\mathbf{k}, i\omega_n)$, where the two terms are the coherent and incoherent parts, respectively. The coherent part provides a sharp contribution to the spectral function $A_d \propto \text{Im} G_d(\mathbf{k}, i\omega_n \to \omega + i\epsilon)$, while the incoherent part is smeared out by the convolution.

As suggested by the phase diagrams, the QAH* phase is only unstable to the band insulator, so it is interesting to see how the spectral functions change as the system approaches the QAH*. We compute the spectral functions at two points marked by the two stars in Fig. 3(a); one point is deep in the band insulator, while the other is close to a transition to QAH*. Figure 7 shows the spectral functions of the electrons in layer 1 (layer 2) denoted by $A_{c(d)}$, while the subscript "coherent" denotes the coherent part. They are obtained from a calculation on a cylinder with zigzag edges using the self-consistent bulk Hamiltonians. In the calculation, the Green functions are computed from electron operators located close to a boundary of the system.

Deep in the band insulator phase, the gap at $\omega = 0$ in the edge states is the result of a hybridization between the electronic and the spinon edge modes (upper panels of Fig. 7).

The signature of the left moving and right moving edge modes are still fairly apparent despite the hybridization effect. In contrast, near the transition to QAH* (lower panels), the hybridization is strongly suppressed, so the edge mode in the bottom left panel is almost unaffected, and thus resembles that of a Chern insulator. Meanwhile, $A_{d,\text{coherence}}$ progressively fades away in both the in-depth states (the continuum) and the edge state (in-gap state). We conclude the section by noting that such a small hybridization near the phase boundary may lead to an incorrect characterization of the system in experiments. For instance, if electrons can undergo Landau-Zener tunneling across the hybridization gap, one might incorrectly conclude that the system exhibits a QAH effect despite the trivial band topology.

VI. SUMMARY

We have studied a bilayer Haldane model under the effect of electron correlations as a lattice Anderson version of the topological bootstrap. Using slave rotor theory, we have explored the phase diagram of this model, and have found a fractionalized quantum anomalous Hall insulator arising from a trivial insulator which undergoes a layer-selective Mott transition in the strongly correlated regime. This phase has coexisting electronic and semionic bulk excitations and is predicted to exhibit a combination of a quantized electrical Hall effect and a quantized thermal Hall effect which violates the Wiedemann-Franz law due to fractionalization. The hybridization can drive QAH* into a topologically trivial insulator, which can be viewed as a Kondo insulator in the strong-coupling limit. However, it is not a direct transition in the current model; a direct transition between QAH* and the trivial insulator may be achieved by adding other microscopic terms, which we leave for future studies.

APPENDIX A: ORIGIN OF THE DIRAC POINTS

The Dirac points arise at the momenta where the fermionic Bloch Hamiltonian of $H_{f,c}$ can be written in a special form: *The first diagonal block differs from the second one by a rescaling and a constant,* namely:

$$\mathcal{H}_{c,f}(\mathbf{k}) = \begin{pmatrix} \alpha + \gamma \mathcal{H}_1(\mathbf{k}) & V \\ V & \mathcal{H}_1(\mathbf{k}) \end{pmatrix}$$

$$= V\tau_x + \frac{\alpha + (\gamma - 1)\mathcal{H}_1(\mathbf{k})}{2}\tau_z$$

$$+ \frac{\alpha + (\gamma + 1)\mathcal{H}_1(\mathbf{k})}{2}\tau_0,$$

(A1)

where $\mathcal{H}_1$ is a two-by-two matrix, V, α, γ are constant, and τ's are Pauli matrices acting on the layer index. To see this, we first start with the general form of the Bloch Hamiltonian with nearest- and next-nearest-neighbor hoppings in the basis
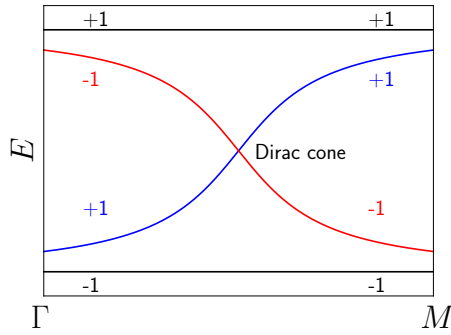
FIG. 8. Schematic band structure along a Γ-M line illustrating the presence of a Dirac cone. The ± 1 are the eigenvalues of the matrix $\mathcal{U}(\mathbf{k})$.

of $(f_{\mathbf{k}A\sigma}, f_{\mathbf{k}B\sigma}, c_{\mathbf{k}A\sigma}, c_{\mathbf{k}B\sigma})^T$,

$$
\mathcal{H}_{c,f}(\mathbf{k}) = \begin{pmatrix} \alpha + \beta\mathcal{H}_1(\mathbf{k}) + \gamma\mathcal{H}_2(\mathbf{k}) & V \\ V & \mathcal{H}_1(\mathbf{k}) + \gamma'\mathcal{H}_2(\mathbf{k}) \end{pmatrix},
$$
(A2)

where $\mathcal{H}_1$ and $\mathcal{H}_2$ are 2×2 matrices originating from the nearest- and next-nearest-neighbor hoppings, respectively. $\alpha, \beta, \gamma, \gamma'$ are constant, while V is the hybridization term. We have switched the order of the layer for simplicity, and the $f^\dagger$ operator can either be electron or spinon in layer 2.

The special form in Eq. (A1) is obtained when $\mathcal{H}_2(\mathbf{k}) = 0$. In the Haldane model, the block $\mathcal{H}_2(\mathbf{k}) = -t_2\sigma_z \sum_\mu \sin(\mathbf{k} \cdot \mathbf{b}_\mu)$ is diagonal and real valued, where σ acts on the sublattice index. $\mathbf{b}_\mu$'s are the three vectors connecting a site with its next-nearest neighbors in the honeycomb lattice. Hence the special form can occur on a (set of) curve, i.e., a 1D object, in the BZ as the result of solving an equation with two unknowns. When the inversion breaking term is absent, the

1D object consists of the Γ-M lines. We should restrict the discussion below to this special case for simplicity. Consider a matrix,

$$
\mathcal{S}(\mathbf{k}) = V\tau_x + \frac{\alpha + (\gamma - 1)\mathcal{H}_1(\mathbf{k})}{2}\tau_z,
$$
(A3)

which is just the first two terms in (A1). Clearly $\mathcal{S}(\mathbf{k})$ commutes with $\mathcal{H}_{c,f}(\mathbf{k})$ so the Bloch wave functions on the Γ-M lines are also eigenfunctions of $\mathcal{S}(\mathbf{k})$. Define another matrix which take the signs of the eigenvalues of $\mathcal{S}(\mathbf{k})$, $\mathcal{U}(\mathbf{k}) = \mathrm{Sgn}(\mathcal{S}(\mathbf{k}))$. Then the formation of the Dirac cones can be understood as the crossing of the bands with ± 1 eigenvalues of $\mathcal{U}(\mathbf{k})$ along the Γ-M lines as illustrated in Fig. 8. Another way to understand the Dirac cones is to impose another constraint on the eigenvalues of $\mathcal{H}_{c,f}(\mathbf{k})$ of the special form such that the middle two bands have an equal energy. We have two variables, k_x and k_y, to tune in order to satisfy the two equations, hence the Dirac cones can exist at multiple points on the Γ-M lines of the BZ.

The form of $\mathcal{S}(\mathbf{k})$ can hint a way to gap out the Dirac points. One example is to introduce third-nearest-neighbor hoppings, forbidding the special form, thereby gapping out the Dirac cones.

APPENDIX B: NONLINEAR SIGMA MODEL REPRESENTATION OF ROTOR MEAN-FIELD HAMILTONIAN

Here we briefly outline the computation of the rotor bond mean fields in (12)–(17). They are computed using a Euclidean action constructed from the rotor Hamiltonian H_θ which is then represented by a nonlinear sigma model. The nonlinear sigma model representation is quadratic and is used to compute the bond mean fields. The Euclidean action constructed from H_θ is given by

$$
S_E[L, \theta] = \int_0^\beta d\tau \left[\sum_i \left(-iL_i\partial_\tau\theta_i + \lambda_i L_i + \frac{U}{2}L_i^2 \right) + \left(\sum_{\langle ij \rangle} -2t_1 F_{nn}e^{-i\theta_i}e^{i\theta_j} - \sum_i 2t_\perp F_{\perp,i}e^{-i\theta_i} + \text{c.c.} \right) \right]
$$
$$
+ \int_0^\beta d\tau \left(\sum_{\langle\langle ij \rangle\rangle} -2t_2 F_{nnn,i}e^{-i\theta_i}e^{i\theta_j}e^{-i\nu_{ij}(\phi+\varphi_i)} + \text{c.c.} \right),
$$
(B1)

where the partition function $\mathcal{Z} = \int \mathcal{D}\theta\mathcal{D}L \exp(-S_E)$. Integrating out the angular momentum field, we obtain

$$
S_E[L, \theta] = \int_0^\beta d\tau \left[\sum_i \left(\frac{(\partial_\tau\theta_i)^2}{2U} + \lambda_i\frac{i\partial_\tau\theta}{U} \right) + \left(\sum_{\langle ij \rangle} -2t_1 F_{nn}e^{-i\theta_i}e^{i\theta_j} - \sum_i 2t_\perp F_{\perp,i}e^{-i\theta_i} + \text{c.c.} \right) \right]
$$
$$
+ \int_0^\beta d\tau \left[\sum_{\langle\langle ij \rangle\rangle} -2t_2 F_{nnn,i}e^{-i\theta_i}e^{i\theta_j}e^{-i\nu_{ij}(\phi+\varphi_i)} + \text{c.c.} \right].
$$
(B2)

Replacing the phase factor by a sigma field $X = e^{i\theta}$ whose constraint $|X_i|^2 = 1$ is imposed using two Lagrange multipliers $\rho_{A(B)}$. One arrives at a nonlinear sigma model of the rotor Hamiltonian:

$$
S_E[X^*, X] = \int_0^\beta d\tau \left[\sum_i \left(\frac{|\partial_\tau X_i|^2}{2U} + \frac{\lambda_i}{2U}(X_i^*\partial_\tau X_i - \partial_\tau X_i^* X_i) \right) + \left(\sum_{\langle ij \rangle} -2t_1 F_{nn}X_i^* X_j - \sum_i 2t_\perp F_{\perp,i}X_i^* + \text{c.c.} \right) \right]
$$
$$
+ \int_0^\beta d\tau \left[\sum_{\langle\langle ij \rangle\rangle} \left(-2t_2 F_{nnn,i}X_i^* X_j e^{-i\nu_{ij}(\phi+\varphi_i)} + \text{c.c.} \right) + \sum_i \rho_i X_i^* X_i \right].
$$
(B3)

This is a quadratic action which can be used to compute the bond mean fields. In the Fourier space $(\mathbf{k}, i\omega_n)$, the action is given by

$$S_E = \sum_{\mathbf{k},n,s,s'} X^*_{\mathbf{k},n,s} \mathcal{S}_{s,s'}(\mathbf{k}, \omega_n) X_{\mathbf{k},n,s'} - \sum_s 2t_\perp F_{\perp,s} \sqrt{\beta N_c}(X_{0,0,s} + \text{c.c.}), \tag{B4}$$

$$\mathcal{S}_{s,s'}(\mathbf{k}, \omega_n) = \begin{pmatrix} \frac{\omega_n^2}{2U} + \frac{\lambda_A}{U}i\omega_n + \rho_A & \\ & \frac{\omega_n^2}{2U} + \frac{\lambda_B}{U}i\omega_n + \rho_B \end{pmatrix} + \mathcal{H}^X_{s,s'}(\mathbf{k}), \tag{B5}$$

where N_c is the number of unit cell in layer 2; s, s' are sublattice indices and $\mathcal{H}^X_{s,s'}(\mathbf{k})$ originates from the in-plane hopping terms in Fourier space which does not depend on the frequency. We have added the inversion symmetry breaking term (only present explicitly in the fermionic sector), which leads to two sigma fields to account for the charge imbalance in a generic case. Two λ's and two ρ's are needed as a consequence.

The following propagator is essential for solving the self-consistent conditions:

$$\langle X_{\mathbf{k},\omega_n,s} X^\dagger_{\mathbf{k},\omega_n,s'} \rangle = \mathcal{S}^{-1}_{s,s'}(\mathbf{k}, \omega_n) + \delta_{\mathbf{k},0}\delta_{\omega_n,0}\langle X_{0,0,s} \rangle \langle X^*_{0,0,s'} \rangle, \tag{B6}$$

where $\langle X_{0,0,s} \rangle = \sum_{s'} 2t_\perp \sqrt{\beta N_c} \, \mathcal{S}^{-1}(0,0)_{s,s'} F_{\perp,s'}$. To satisfy the sigma field constraints, we impose the following conditions:

$$1 = \frac{1}{N_c} \sum_i \langle X^\dagger_{is}(\tau = \epsilon) X_{is}(0) \rangle = \frac{1}{\beta N_c} \sum_{\mathbf{k},n} \langle X^\dagger_{\mathbf{k}\omega_n s} X_{\mathbf{k}\omega_n s} \rangle e^{-i\omega_n \epsilon}, \tag{B7}$$

where $\epsilon \to 0^+$ is to keep the correct ordering of the operators. To compute the frequency sum, we use the residue theorem to convert the sum over the poles of the Bose function $n_B(z) = \frac{1}{e^{\beta z}-1}$ into a pole sum of a function $f(\mathbf{k}, z) \overset{i\omega_n \to z}{=} \langle X^\dagger_{\mathbf{k}\omega_n s} X_{\mathbf{k}\omega_n s} \rangle$. We compute the poles of $f(\mathbf{k}, z)$ numerically and obtain the frequency sum. The Hilbert space constraints can be expressed similarly in terms of the propagator in Eq. (B6). They involve the expectation values of the angular momentum obtained from a Heisenberg equation of the rotor operator $\partial_\tau X_{is} = [H_\theta, X_{is}(\tau)]$ and the commutator $[L, e^{i\theta}] = e^{i\theta}$:

$$L_{is} = -\frac{\lambda_s}{U} - \frac{1}{2} + \frac{1}{U} X^\dagger_{is} \frac{\partial X_{is}}{\partial \tau}. \tag{B8}$$

Likewise, the bond mean fields in (12)–(17) can also be computed using the pole summation procedure described above.

[1] T. H. Hsieh, H. Ishizuka, L. Balents, and T. L. Hughes, Phys. Rev. Lett. **116**, 086802 (2016).

[2] M. Z. Hasan and C. L. Kane, Rev. Mod. Phys. **82**, 3045 (2010).

[3] T. H. Hsieh, Y.-M. Lu, and A. W. W. Ludwig, Sci. Adv. **3**, e1700729 (2017).

[4] V. Kalmeyer and R. B. Laughlin, Phys. Rev. Lett. **59**, 2095 (1987).

[5] X. G. Wen, F. Wilczek, and A. Zee, Phys. Rev. B **39**, 11413 (1989).

[6] X. G. Wen, Int. J. Mod. Phys. B **04**, 239 (1990).

[7] D. F. Schroeter, E. Kapit, R. Thomale, and M. Greiter, Phys. Rev. Lett. **99**, 097202 (2007).

[8] R. Thomale, E. Kapit, D. F. Schroeter, and M. Greiter, Phys. Rev. B **80**, 104406 (2009).

[9] C.-X. Liu, S.-C. Zhang, and X.-L. Qi, Annu. Rev. Condens. Matter Phys. **7**, 301 (2016).

[10] M. Hohenadler and F. F. Assaad, J. Phys.: Condens. Matter **25**, 143201 (2013).

[11] J. Maciejko and G. A. Fiete, Nat. Phys. **11**, 385 (2015).

[12] M. Dzero, J. Xia, V. Galitski, and P. Coleman, Annu. Rev. Condens. Matter Phys. **7**, 249 (2016).

[13] K. Jiang, S. Zhou, X. Dai, and Z. Wang, Phys. Rev. Lett. **120**, 157205 (2018).

[14] D. Pesin and L. Balents, Nat. Phys. **6**, 376 (2010).

[15] S. Rachel and K. Le Hur, Phys. Rev. B **82**, 075106 (2010).

[16] T. Senthil, S. Sachdev, and M. Vojta, Phys. Rev. Lett. **90**, 216403 (2003).

[17] J. Maciejko and A. Rüegg, Phys. Rev. B **88**, 241101(R) (2013).

[18] R. Nandkishore, M. A. Metlitski, and T. Senthil, Phys. Rev. B **86**, 045128 (2012).

[19] S. Florens and A. Georges, Phys. Rev. B **66**, 165111 (2002).

[20] S. Florens and A. Georges, Phys. Rev. B **70**, 035114 (2004).

[21] S.-S. Lee and P. A. Lee, Phys. Rev. Lett. **95**, 036403 (2005).

[22] E. Zhao and A. Paramekanti, Phys. Rev. B **76**, 195101 (2007).

[23] D. Podolsky, A. Paramekanti, Y. B. Kim, and T. Senthil, Phys. Rev. Lett. **102**, 186401 (2009).

[24] C. Hickey, L. Cincio, Z. Papić, and A. Paramekanti, Phys. Rev. Lett. **116**, 137202 (2016).

[25] F. D. M. Haldane, Phys. Rev. Lett. **61**, 2015 (1988).

[26] H.-H. Lai, S. E. Grefe, S. Paschen, and Q. Si, Proc. Natl. Acad. Sci. U.S.A. **115**, 93 (2018).

[27] R. Nakai, S. Ryu, and K. Nomura, Phys. Rev. B **95**, 165405 (2017).

[28] J. He, S.-P. Kou, Y. Liang, and S. Feng, Phys. Rev. B **83**, 205116 (2011).

[29] X. G. Wen, Phys. Rev. B **43**, 11025 (1991).

[30] C. L. Kane and M. P. A. Fisher, Phys. Rev. B **55**, 15832 (1997).

[31] X.-Y. Feng, J. Dai, C.-H. Chung, and Q. Si, Phys. Rev. Lett. **111**, 016402 (2013).